Nonlinear mode conversion with chaotic soliton generation at plasma resonance

H. Pietsch, E. W. Laedke, and K. H. Spatschek
Institut für Theoretische Physik I, Heinrich-Heine Universität Düsseldorf, D-4000 Düsseldorf, Germany
(Received 3 August 1992)

The resonant absorption of electromagnetic waves near the critical density in inhomogeneous plasmas is studied. A driven nonlinear Schrödinger equation for the mode-converted oscillations is derived by multiple-scaling techniques. The model is simulated numerically. The generic transition from a stationary to a time-dependent solution is investigated. Depending on the parameters, a time-chaotic behavior is found. By a nonlinear analysis, based on the inverse scattering transform, solitons of a corresponding integrable equation are identified as the dominant coherent structures of the chaotic dynamics. Finally, a map is presented which predicts chaotic soliton generation and emission at the critical density. Its qualitative behavior, concerning the bifurcation points, is in excellent agreement with the numerical simulations.

PACS number(s): 52.35.Sb, 52.35.Mw, 05.45.+b

I. INTRODUCTION

The interaction of intense electromagnetic radiation with inhomogeneous plasmas is a subject of considerable interest in several physical applications. We mention, e.g., laser-plasma interaction experiments related to controlled fusion [1], or microwave interaction with plasmas [2]. In the present investigation we consider the problem of resonant absorption of electromagnetic waves. Let us have oblique incidence onto an inhomogeneous plasma with weak gradients. Resonant absorption takes place at the so-called "critical density," where the frequency of the electromagnetic wave coincides with the local plasma frequency. There the electromagnetic wave is converted into an electrostatic plasma wave [3–5]. Without damping, the wave energy convection, due to the propagation of the plasma wave towards the low-density region of the plasma, becomes important, whereas for strong damping, the plasma-wave convection can be neglected [6].

The linear approximation, when the plasma density is not modified, breaks down even for relatively weak intensities of the incoming wave since the amplitude of the resonant plasma wave can reach large values in comparison to the incident electromagnetic wave [3]. Then the ponderomotive force associated with the high-frequency electrostatic field is non-negligible and leads to nonlinear modifications of the density profile. Extensive studies of the resonant absorption during the past years show interesting dynamical behavior of the plasma wave near the resonance point. In the linear approximation, the steady-state solution is the modified Airy function [3]. For the more realistic model, including ponderomotive force effects, the solution of the model equation—the driven nonlinear inhomogeneous Schrödinger equation (DNLIS)—bifurcates from the steady-state regime into time-dependent solutions. Adam, Serveniere, and Lavale [7] observed periodic emission of localized wave packets in one region of the parameter space, whereas for strong driving fields the emission is less organized. The generation of localized wave packets has also been experimentally confirmed [8].

In this paper we describe the creation and the emission of localized pulses from the critical density. In Sec. II we derive, with a multiple-scaling technique, the model equation from a two-fluid description of the plasma. The results of extensive numerical simulations of the model are presented in Sec. III. They clarify the transition from the stationary state to a time-dependent attractor in the chaotic regime. The route to chaos is identified by specific diagnostics. In Sec. IV we examine the spatial structures of the numerically observed solutions by a nonlinear analysis. The algorithm is based on the inverse scattering transform (IST) for the integrable equation, which corresponds to the model equation if the driving magnetic field is neglected. We show that the localized pulses can be described, from their creation at the critical density up to their asymptotic-time behavior, by the multisoliton-solution of the cubic nonlinear Schrödinger equation. The results of Secs. III and IV indicate that the complex time-dependent behavior can be modeled by a low-dimensional system. In Sec. V we present such a low-dimensional model, which describes the chaotic soliton generation at the critical density. For nearly all bifurcation points we get an excellent agreement with the numerical simulation. A brief summary is given in Sec. VI.

II. MODEL EQUATION

In this section we derive by multiple-scaling techniques a simplified model equation. It describes the nonlinear coupling between high-frequency, nearly electrostatic processes and the low-frequency plasma dynamics in the case of resonant absorption of electromagnetic waves in fully ionized inhomogeneous plasmas. As illustrated in Fig. 1 we consider a plane electromagnetic wave being obliquely incident onto an inhomogeneous plasma with a density gradient in the x direction. The electric-field vector $\mathbf{E}$ lies in the x,y plane, which also contains the wave vector $\mathbf{k}_0$ of the incident (p polarized) wave; θ_0 is the angle of incidence.

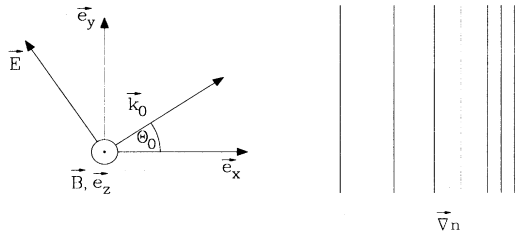

FIG. 1. Oblique incident of electromagnetic waves.

If we consider physical situations where the characteristic length L of the density gradient is much larger than both the Debye length λ_D and the wavelength of the incident wave $|\mathbf{k}_0|^{-1}$ we can restrict our analysis to the vicinity of the critical point x_c. At the latter the wave frequency ω_0 of the incident wave coincides with the local plasma frequency ω_p, and we approximate the plasma density by

$$n_0 = n_c \left[1 + \frac{x}{L} \right] . \tag{1}$$

In (1) we have chosen $x_c = 0$. Following the linear theory, which is summarized in Ref. [3], we find that (i) the incident wave is reflected at a position x_r given by $\omega_{pe}(x_r) = \omega_0 \cos\theta_0$, and (ii) that in the resonance region near $x = 0$ the main electric field is electrostatic and parallel to the density gradient. In the cold inhomogeneous plasma situation one obtains at the resonance position a singularity of the mode-converted electric field [23]. This unphysical singularity is removed by collisions, thermal convection, or nonlinear effects [5,9]. In the case of, e.g., a thermal plasma,

$$|E_x|_{\max} \approx \left[\frac{L}{\sqrt{3}\lambda_{De}} \right]^{2/3} \frac{|E_I|}{\sqrt{2\pi k_0 L}} \Phi(\xi) \tag{2}$$

holds for the electric field at $n_0(0) = n_c$. In (2) $|E_I|$ is the amplitude of the incident electromagnetic wave and $\Phi(\xi)$ is the Ginzburg-function [3], with $\xi = (k_0 L)^{1/3} \sin(\theta_0)$. The maximum value of $\Phi(\xi)$ is in the range $0.5° < \theta_0 < 3°$ and for a typical experiment [8] we find from (2) $|E_x|_{\max} \approx 30 |E_I|$.

This result of the linear theory calls for a nonlinear theory, which was first presented by Adam, Serveniere, and Lavale [7]. In their derivation of a DNLIS equation, they assumed that the tunneling component of the magnetic field is constant near the critical density. To verify this assumption one can use a multiple-scale formalism. Let us present the general outline of such a procedure.

We start with the two-fluid description and introduce dimensionless quantities via

$$\tilde{t} = \frac{\omega_0}{2} t , \tag{3}$$

$$\tilde{\mathbf{x}} = \frac{1}{\sqrt{3}\lambda_D} \mathbf{x} , \tag{4}$$

$$\tilde{n}_\alpha = \frac{n_\alpha}{n_c} , \tag{5}$$

$$\tilde{\mathbf{v}}_\alpha = \frac{\mathbf{v}_\alpha}{v_{Te}} , \tag{6}$$

$$\tilde{\mathbf{E}} = \frac{\mathbf{E}}{\left[16\pi n_c \left[1 + \frac{m_e}{m_i} \right] T_e \right]^{1/2}} , \tag{7}$$

$$\tilde{\mathbf{B}} = \frac{\mathbf{B}}{\left[16\pi n_c \left[1 + \frac{m_e}{m_i} \right] T_e \right]^{1/2}} , \tag{8}$$

where the index $\alpha = i, e$ denotes ion and electron contributions, respectively; n_α, $\mathbf{v}_\alpha$, m_α, and $q_\alpha (q_e = -e)$ are the density, velocity, mass, and charge of the species α. The temperature T_α is given in eV and the ratio of the specific heats is denoted later on by γ_α. Truncating in the usual manner, we can write

$$\partial_{\tilde{t}} \tilde{n}_\alpha + \frac{2}{\sqrt{3}} \tilde{\nabla} \cdot (\tilde{n}_\alpha \tilde{\mathbf{v}}_\alpha) = 0 , \tag{9}$$

$$\partial_{\tilde{t}} \tilde{\mathbf{v}}_\alpha + \frac{2}{\sqrt{3}} (\tilde{\mathbf{v}}_\alpha \cdot \tilde{\nabla}) \tilde{\mathbf{v}}_\alpha = \frac{4 m_e q_\alpha}{e m_\alpha} \left[\tilde{\mathbf{E}} + \frac{v_{Te}}{c} \tilde{\mathbf{v}}_\alpha \times \tilde{\mathbf{B}} \right] - \frac{2\gamma_\alpha T_\alpha}{\sqrt{3} v_{Te}^2 m_\alpha n_\alpha} \tilde{\nabla} \tilde{n}_\alpha , \tag{10}$$

$$\tilde{\nabla} \times \tilde{\mathbf{B}} = \frac{\sqrt{3} v_{Te}}{2c} \left[\left[1 + \frac{m_e}{m_i} \right]^{-1} (\tilde{n}_i \tilde{\mathbf{v}}_i - \tilde{n}_e \tilde{\mathbf{v}}_e) + \partial_{\tilde{t}} \tilde{\mathbf{E}} \right] , \tag{11}$$

$$\tilde{\nabla} \times \tilde{\mathbf{E}} = - \frac{\sqrt{3} v_{Te}}{2c} \partial_{\tilde{t}} \tilde{\mathbf{B}} , \tag{12}$$

$$\tilde{\nabla} \cdot \tilde{\mathbf{E}} = \frac{\sqrt{3}}{2} \left[1 + \frac{m_e}{m_i} \right]^{-1} (\tilde{n}_i - \tilde{n}_e) , \tag{13}$$

where we introduced the electron thermal velocity v_{Te} and the electron Debye length $\lambda_D \equiv v_{Te}/\omega_0$. The resonance frequency $\omega_p(x_c)$ is given by

$$\omega_0 = \omega_p(x_c) = [\omega_{pe}^2(x_c) + \omega_{pi}^2(x_c)]^{1/2} , \tag{14}$$

where ω_{pe} and ω_{pi} are the plasma frequencies of electrons and ions, respectively. If one chooses (as mostly done in the literature) $\omega_0 = \omega_{pe}(x_c)$, the resonance position is shifted by an amount proportional to m_e/m_i.

In the following we distinguish between the high-frequency and the low-frequency time scales, and split each quantity in its high- and low-frequency parts, e.g.,

$$\tilde{n}_\alpha = \tilde{n}_0(\tilde{x}) + \tilde{n}_\alpha^L + \tilde{n}_\alpha^H . \tag{15}$$

This is the starting point for the scaling. We assume the incident electromagnetic wave to be of small amplitude $[|E_I| \approx \delta^2 \leq 1]$, with

$$\delta \equiv (\sqrt{3} \lambda_D L^{-1})^{1/3} , \tag{16}$$

and make the following ansatz for the high-frequency quantities:

$$\tilde{n}_e^H = \mathrm{Re}\{ [\delta^2 \bar{n}_e^{H0}(\delta\tilde{x}, \delta^4 \tilde{y}, \delta^2 \tilde{t}) + \cdots] \exp(\cdots) \} , \tag{17}$$

$$\tilde{n}_i^H=\mathrm{Re}\left\{\frac{m_e}{m_i}[\delta^2\bar{n}_i^{H0}(\delta\bar{x},\delta^4\bar{y},\delta^2\bar{t})+\cdots]\exp(\cdots)\right\}, \tag{18}$$

$$\tilde{v}_{e\bar{x}}^H=\mathrm{Re}\{[\delta\bar{v}_{e\bar{x}}^{H0}(\delta\bar{x},\delta^4\bar{y},\delta^2\bar{t})+\delta^3\bar{v}_{e\bar{x}}^{H1}(\delta\bar{x},\delta^4\bar{y},\delta^2\bar{t})+\cdots]\exp(\cdots)\}, \tag{19}$$

$$\tilde{v}_{e\bar{y}}^H=\mathrm{Re}\left\{\frac{v_{Te}}{c}[\delta\bar{v}_{e\bar{y}}^{H0}(\delta\bar{x},\delta^4\bar{y},\delta^2\bar{t})+\cdots]\exp(\cdots)\right\}, \tag{20}$$

$$\tilde{v}_{i\bar{x}}^H=\mathrm{Re}\left\{\frac{m_e}{m_i}[\delta\bar{v}_{i\bar{x}}^{H0}(\delta\bar{x},\delta^4\bar{y},\delta^2\bar{t})+\cdots]\exp(\cdots)\right\}, \tag{21}$$

$$\tilde{v}_{i\bar{y}}^H=\mathrm{Re}\left\{\frac{m_e v_{Te}}{m_i c}[\delta\bar{v}_{i\bar{y}}^{H0}(\delta\bar{x},\delta^4\bar{y},\delta^2\bar{t})+\cdots]\exp(\cdots)\right\}, \tag{22}$$

$$\tilde{E}_{\bar{x}}^H=\mathrm{Re}\{[\delta\bar{E}_{\bar{x}}^{H0}(\delta\bar{x},\delta^4\bar{y},\delta^2\bar{t})+\delta^3\bar{E}_{\bar{x}}^{H1}(\delta\bar{x},\delta^4\bar{y},\delta^2\bar{t})+\cdots]\exp(\cdots)\}, \tag{23}$$

$$\tilde{E}_{\bar{y}}^H=\mathrm{Re}\left\{\frac{v_{Te}}{c}[\delta\bar{E}_{\bar{y}}^{H0}(\delta\bar{x},\delta^4\bar{y},\delta^2\bar{t})+\cdots]\exp(\cdots)\right\}, \tag{24}$$

$$\tilde{B}_{\bar{z}}^H=\mathrm{Re}\{[\delta^2\bar{B}_{\bar{z}}^{H0}(\delta\bar{x},\delta^4\bar{y},\delta^2\bar{t})+\cdots]\exp(\cdots)\}. \tag{25}$$

For the reason of lucidity we presented in (17)–(25) only the lowest orders and introduced the abbreviation

$$\exp(\cdots)\equiv\exp\left[i\left[\sqrt{3}\frac{v_{Te}}{c}\alpha_0\bar{y}-2\bar{t}\right]\right], \tag{26}$$

with $\alpha_0\equiv\sin(\theta_0)$. For the low-frequency quantities, we assume

$$\tilde{n}_e^L=\delta^2\bar{n}_e^{L0}(\delta\bar{x},\delta^4\bar{y},\delta^2\bar{t})+\cdots, \tag{27}$$

$$\tilde{n}_i^L=\delta^2\bar{n}_i^{L0}(\delta\bar{x},\delta^4\bar{y},\delta^2\bar{t})+\cdots, \tag{28}$$

$$\tilde{\mathbf{v}}_e^L=\frac{m_e}{m_i}\delta\bar{v}_{e\bar{x}}^{L0}(\delta\bar{x},\delta^4\bar{y},\delta^2\bar{t})\mathbf{e}_{\bar{x}}+\cdots, \tag{29}$$

$$\tilde{\mathbf{v}}_i^L=\frac{m_e}{m_i}\delta\bar{v}_{i\bar{x}}^{L0}(\delta\bar{x},\delta^4\bar{y},\delta^2\bar{t})\mathbf{e}_{\bar{x}}+\cdots, \tag{30}$$

$$\tilde{\mathbf{E}}=\delta^3\bar{E}_{\bar{x}}^{L0}(\delta\bar{x},\delta^4\bar{y},\delta^2\bar{t})\mathbf{e}_x+\cdots, \tag{31}$$

$$\tilde{\mathbf{B}}=\delta^5\bar{B}_{\bar{x}}^{L0}(\delta\bar{x},\delta^4\bar{y},\delta^2\bar{t})\mathbf{e}_{\bar{x}}+\cdots. \tag{32}$$

If, in addition, we scale

$$\alpha_0\approx\delta\ ,\quad v_{Te}/c\approx\delta^2\ ,\quad \sqrt{m_e/m_i}\approx\delta\ , \tag{33}$$

introduce the slowly varying variables

$$\bar{x}=\delta\bar{x}\ ,\quad \bar{y}=\delta^4\bar{y}\ ,\quad \bar{t}=\delta^2\bar{t}\ , \tag{34}$$

and neglect the higher harmonics, we obtain after some algebra in order δ^3

$$(\delta^{-1}\alpha_0)\bar{B}_z^{H0}=i\partial_{\bar{t}}\bar{E}_{\bar{y}}^{H0}+\frac{\gamma_e}{3}\partial_{\bar{x}}^2\bar{E}_{\bar{x}}^{H0}+\bar{n}_e^{L0}\bar{E}_x^{H0}-\bar{x}\bar{E}_x^{H0}\ , \tag{35}$$

$$\partial_{\bar{x}}\bar{B}_z^{H0}=0\ . \tag{36}$$

In analogy to the result for the high-frequency part, we get in order δ^4 for the low-frequency electron density $\bar{n}_e^{L0}=\bar{n}_i^{L0}\equiv\bar{n}_0^{L0}$

$$\left[\tfrac{3}{4}\delta^2\frac{m_i}{m_e}\right]\partial_{\bar{t}}^2\bar{n}^{L0}-\gamma_e\partial_{\bar{x}}^2\bar{n}^{L0}=\partial_{\bar{x}}^2|\bar{E}_{\bar{x}}^{H0}|^2\ . \tag{37}$$

Equations (35) and (36) describe the resonant absorption at the critical density.

Some remarks: By introducing a smaller scaling of the transversal component of the electric field [$E_y\approx(v_{Te}/c)E_x$], we ensure that the magnetic field does not depend (to lowest order) on the longitudinal coordinate, which means that the field $\bar{B}_z^{H0}$ is given by its value at the reflection point and does not vary on the "slow" time scale $\bar{t}$. If one neglects in (35) the nonlinear terms, one obtains the linear theory [5].

Introducing the new variables $q=(\alpha_0B_0/\delta)^{-1}\bar{E}_{\bar{x}}^{H0}$ and $N=(\alpha_0B_0/\delta)^{-2}\bar{n}^{L0}$, we can write

$$i\partial_t q+\partial_x^2 q-(x+pN)q=1\ , \tag{38}$$

$$V^2\partial_t^2N-\partial_x^2N=\partial_x^2|q|^2\ . \tag{39}$$

In (38) and (39) (and also in the rest of this paper), space and time variables are denoted by x and t, respectively. The parameters in the system are defined by

$$V^2=\frac{3}{4}\frac{m_i}{m_e}\delta^2\ , \tag{40}$$

$$p=\left[\frac{\alpha_0B_0}{\delta}\right]^2\ . \tag{41}$$

We have assumed for the high-frequency processes an adiabatic response whereas the (low-frequency) electrons are isothermal. The system (38) and (39) was firstly discussed by Adam, Serveniere, and Lavale [7] and reduces in the case of a homogeneous plasma without driving to the well-known Zakharov equations [10].

If one changes without any additional assumption the scaling in the way that the mass ratio m_e/m_i is proportional to δ, the first term in (39) will drop (during the fact that $V^2\ll1$) and one gets $N=-|q|^2$. Inserting this in (38) we end up with the driven nonlinear inhomogeneous Schrödinger equation (DNLIS)

$$i\partial_t q+\partial_x^2 q+p|q|^2q-xq=1\ . \tag{42}$$

Equation (42) is the basic model for our subsequent investigation of the nonlinear resonant absorption at the critical density in inhomogeneous plasmas.

The derivation by a multiple-scale technique helps to clarify the validity of the model equation. The most interesting point is that in this approximation the whole dynamics of the physical system described by the DNLIS equation depends only on one parameter p, which mea-

sures the ratio between the nonlinear ponderomotive effects and the driving magnetic field.

Before studying the solutions of (42), we refer to some important facts of the model equation. If one neglects the driver in (42) (set the right-hand side equal to zero), the DNLIS equation reduces to the nonlinear inhomogeneous Schrödinger (NLIS) equation

$$i\partial_t q+\partial_x^2 q+p|q|^2 q-xq=0\ , \tag{43}$$

which is integrable by the inverse scattering transform [11]. This is the reason that we call (43) "the corresponding integrable equation." Later on, we shall use the fact that Eq. (43) can be transformed via

$$\tilde{x}=x+t^2\ , \tag{44}$$

$$\tilde{t}=t\ , \tag{45}$$

$$\tilde{q}(\tilde{x},\tilde{t})=\left[\frac{p}{2}\right]^{1/2} q(x,t)\exp[i(xt-\tfrac{2}{3}t^3)]\ , \tag{46}$$

into the well-known integrable NLS equation

$$i\partial_{\tilde{t}}\tilde{q}+\partial_{\tilde{x}}^2+2|\tilde{q}|^2\tilde{q}=0\ . \tag{47}$$

III. TRANSITION TO CHAOS

To clarify the transition (with increasing values of p) from the Airy-type solution [3] in the linear stationary regime to the time-dependent and irregular pulse emission as observed by Adam, Serveniere, and Lavale [7], we simulated the solution of the DNLIS equation numerically. We developed a new nonlinear unitary numerical algorithm of second-order accuracy in time and space, which reduces in the linear limit to the well-known Crank-Nicholson method [12]. Due to the semi-implicit structure there exists no Courant-Friedrich-Levi condition and thus the algorithm is unconditionally stable.

To simulate the behavior of localized wave packets in the infinite system we introduced open-end boundary conditions, which we implemented by artificial damping regions on the left and right side of the physically relevant regime, and in addition a cutoff algorithm beyond the left damping region.

In agreement with the analytical result, the numerical simulation results for $p=0$ in the final asymptotic (in time) solution

$$q_s\simeq-\lim_{t\to\infty} i\int_0^t \exp[-\tfrac{1}{3}\tau^3-ix\tau]d\tau\ .$$

For $p<0.55$, the behavior is only quantitatively modified but qualitatively the same. The solutions are asymptotically stable and of the modified Airy-function type, as shown in Fig. 2. For $x\to\pm\infty$ one gets, as expected, $q_s\simeq x^{-1}+O(x^{-3})$. Remarkable is the fact that all stationary solutions have nonvanishing imaginary parts. Real stationary distributions, which one gets, e.g., by solving the time-independent equation, are unstable.

For $p>0.55$ the dynamical behavior of the system is completely changed. As has been observed by Adam, Serveniere, and Lavale [7], the stationary solutions undergo a modulational instability and for finite values of p

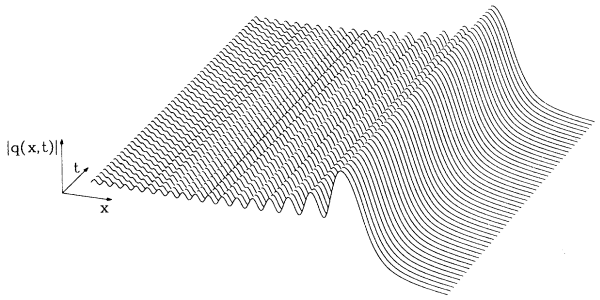

FIG. 2. Stationary Airy-type solution ($p=0.3$).

a new type of solution appears, which is depicted in Fig. 3. It can be described by the following physically motivated picture. A single localized pulse is created near the critical density ($x=0$). Its amplitude grows until its phase decouples from the constant driver. Then the wave packet moves accelerated down the density gradient. After being emitted from the region of critical density the pulse shape adjusts itself to an asymptotic solitonlike structure. From the remaining structure at $x=0$ a new wave packet is created and the procedure described above repeats. The dynamics of the pulse emission is sensitively depending on the parameter p. The behavior beyond the first bifurcation at $p\approx0.55$ was investigated in a series of numerical experiments. Typical results are shown in Figs. 4–7. In each case, we show the frequency spectrum and Poincaré plot $\mathrm{Im}\{q_{n+1}\}$ versus $\mathrm{Im}\{q_n\}$, where $q_n=q(x=0,t=\tau_n)$. The Poincaré times τ_n are defined by the changes of $\mathrm{Re}\{q(x=0)\}$ from negative to positive values.

In the interval $0.55<p<1.08$ the emission of wave packets is periodic. In Fig. 4 we observe one frequency and, of course, its harmonics, whereas in the Poincaré plot a convergence to a fixed point occurs. This corresponds to periodic solutions and to a limit cycle in the reduced phase space $q(x=0,t)$. The emission frequency increases with increasing p.

At $p=1.089$ a period doubling occurs. In the reduced phase space the limit cycle splits up into a two-cycle, and in the frequency spectrum (Fig. 5) a new frequency, at the

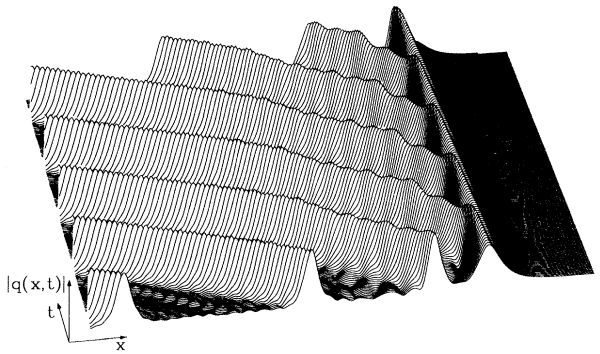

FIG. 3. Regular emission of localized pulses in the dynamical regime ($p=1.0$).

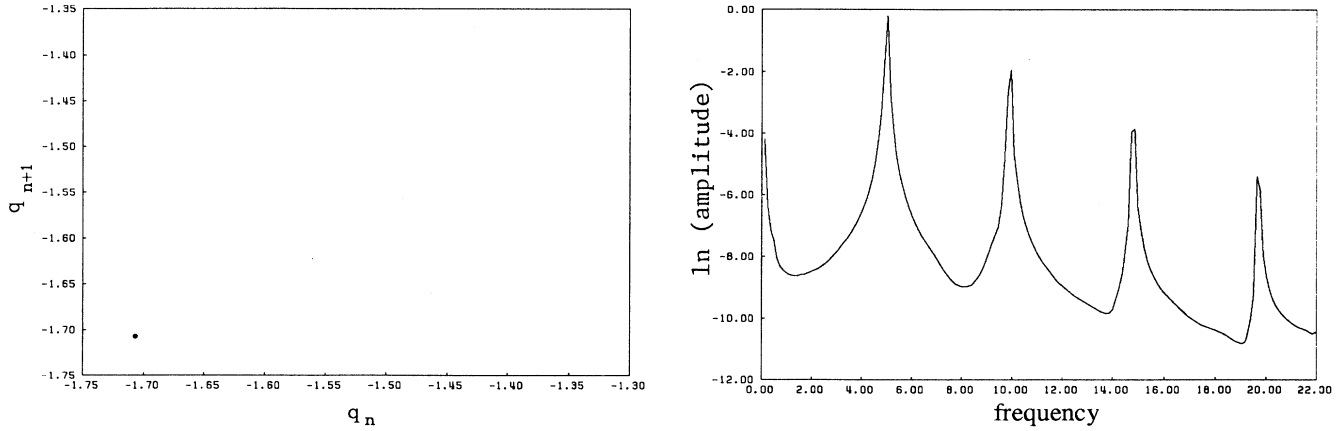

FIG. 4. Poincaré plot and frequency spectrum in the periodic regime (here $p=0.7$).

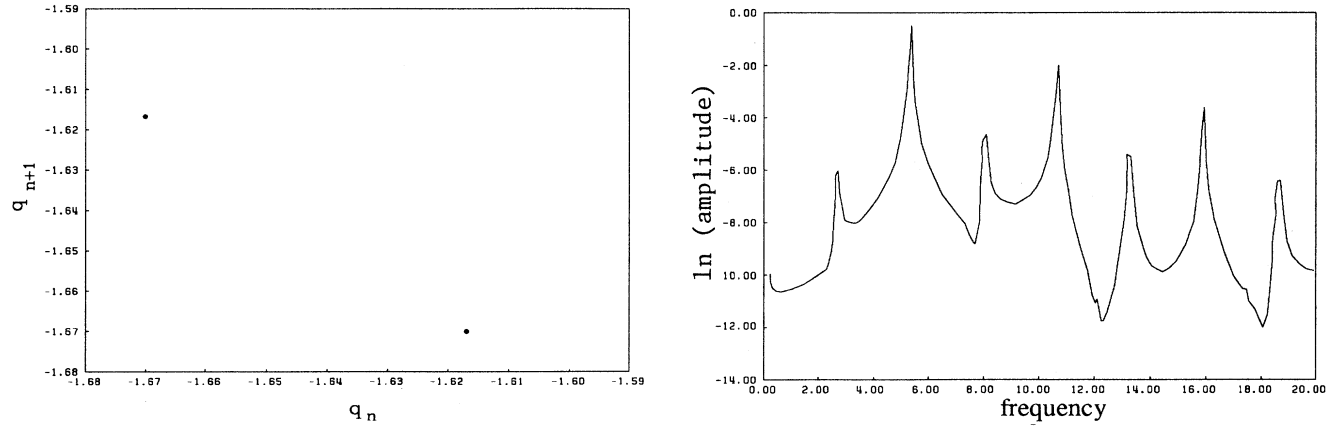

FIG. 5. Same as Fig. 4 for $p=1.1$. A period doubling occurs.

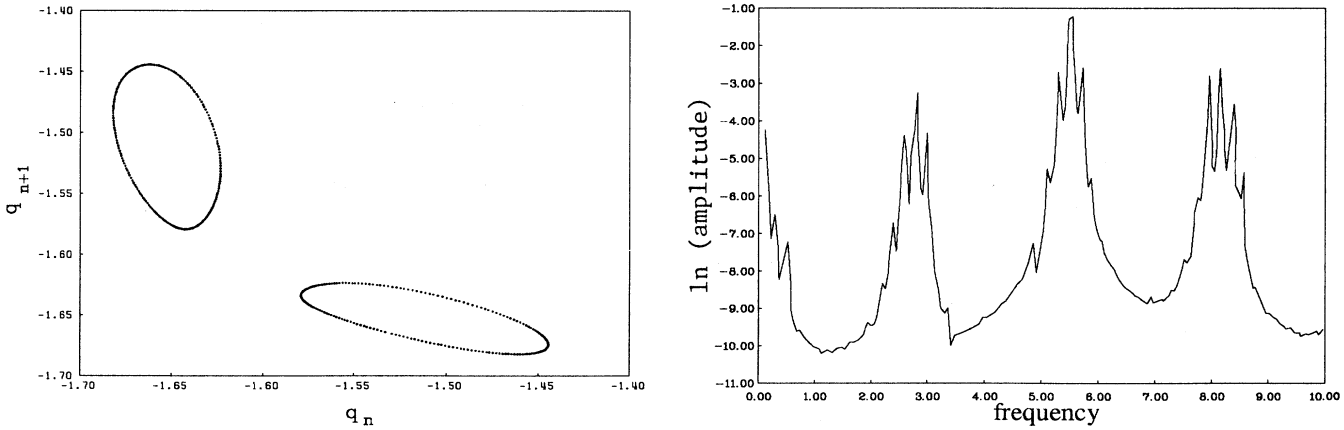

FIG. 6. Same as Fig. 4 for $p=1.16$. A second (incommensurate) frequency appears and leads to satellites in the spectrum. The emission of solitons is quasiperiodic.

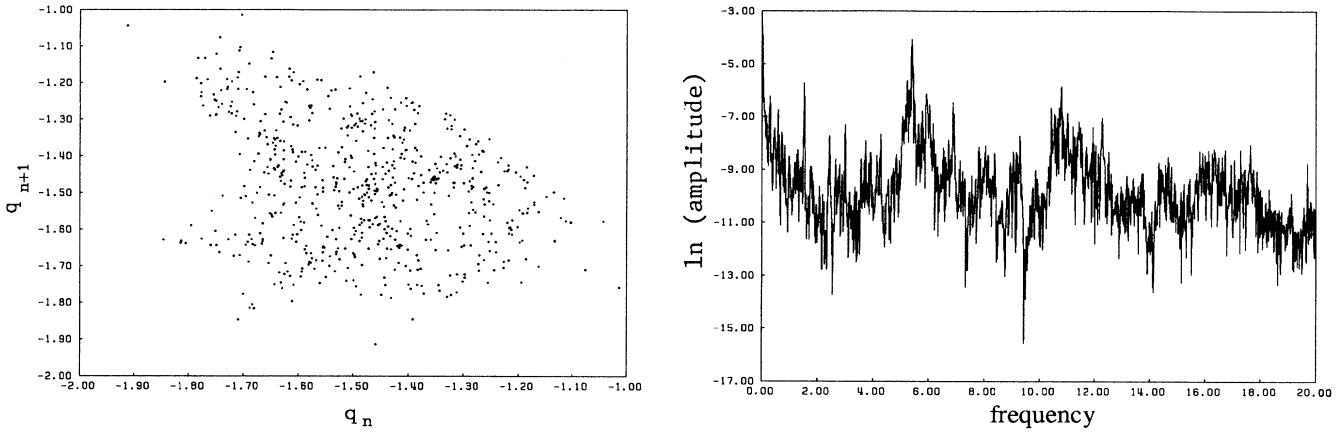

FIG. 7. Same as Fig. 4 for $p=1.27$. The emission of solitons is chaotic.

half of the original one, occurs. This subharmonic bifurcation leads also to a doubling of the original fixed point in the Poincaré plot. The spacing between the fixed points, and also between the corresponding two-cycles, increases with increasing p. The situation is as follows: After the emission of a pulse with lower amplitude a new wave packet is created at the critical density. The new pulse is smaller and has larger amplitude than the previous one. A further increase of the control parameter leads to a different bifurcation cascade as predicted after the first period doubling.

At $p\approx 1.16$, a second, within the numerical accuracy incommensurate, frequency appears. As seen in Fig. 6 this frequency is much smaller than the original one and leads to satellites in the spectrum. In the Poincaré intersection, the two previous fixed points split up and change to circles that will be completely filled with increasing time. In the reduced phase space the two-cycle starts to oscillate and the dynamical behavior is quasiperiodic on a two-torus. The amplitudes and widths of the successively emitted wave packets are all different from each other.

For $p>1.25$ the two-torus breaks down and no regular emission is distinguished. In the frequency spectrum (Fig. 7), we observe a broadband distribution, which indicates chaos. Thus the model system leads to a chaotic attractor according to the Newhouse-Ruelle-Takens [13,14] route to chaos.

We should point out that the behavior described above does not depend on the x point of inspection (which defines the reduced phase space). To check whether the chaotic attractor is of low dimension we determined the correlation dimension D_c [15,16] in the vicinity of $p\approx 1.25$. For the numerical estimation we approximated the exact value of the correlation function $\bar{c}_d(\xi)$ by the method of Ref. [17]. The results are depicted in Fig. 8.

In the periodic and two-periodic regime we obtain $D_c=1$, whereas in the quasiperiodic regime the correlation dimension $D_c=2$ agrees with the dimension of the observed torus. For $p\approx 1.25$ we get $D_c=4.38$ as the fractal dimension of the chaotic attractor. The picture of a quasiperiodic route to chaos for soliton generation at the critical density is meanwhile well established in literature [18–21].

IV. COHERENT SPATIAL STRUCTURE WITHIN CHAOS

The aim of this section is to clarify the spatial structure of the solution and to discuss the observed self-organization of the chaotic system. As was done previously for other nonlinear systems [22], we try to identify solitons of the corresponding integrable equation (the NLIS equation) as the main constituents of the dynamics.

We split the whole x space in two regions. In the first region, the convective regime ($x\ll 0$), all pulses are well-separated; see, e.g., the three left pulses in Fig. 9. Near the critical density (at $x=0$) in the creation region, several pulses overlap. This characteristic behavior is preserved at all times t and for $p\geq 0.55$.

First we discuss the convective region. There, a chain of pulses moves accelerated down the density gradient to regions with lower plasma density. The amplitudes and the widths of the pulses remain constant. For the position x_M of a single pulse as function of time t we found $x_M\approx -t$. The phase of the pulse varies linearly with x for a fixed time. From the fact that the distance between different pulses remains constant it follows that the acceleration is the same for all pulses.

These results lead to the conclusion that the solution of the nonintegrable DNLIS equation in the convective region is mainly a N-soliton solution [23] of the integrable NLIS equation. If the distances between the solitons in the N-soliton solution are very large, the separated solitons approximately decouple and form a chain of single pulses as observed in the numerical simulation. One obtains for each pulse the one-soliton solution

$$q_s(x,t)=\left[\frac{2}{p}\right]^{1/2} 2\eta\,\mathrm{sech}[2\eta(x+t^2+4\xi t-x_0)] \times\exp\{-i[(2\xi+t)x+\tfrac{1}{3}t^3+2\xi t^2 -4(\eta^2-\xi^2)t-\varphi_0]\}\ . \tag{48}$$

The characteristic relations between amplitudes, widths, phases, and positions of the numerically observed pulses are the same as in (48) [see, e.g., Fig. 10]. If we compare the pulses, obtained from numerical simulation, the devi-

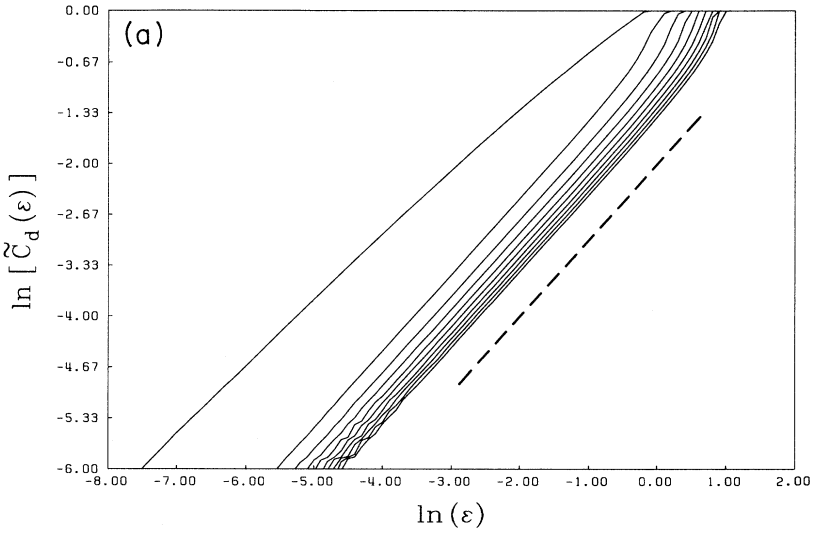

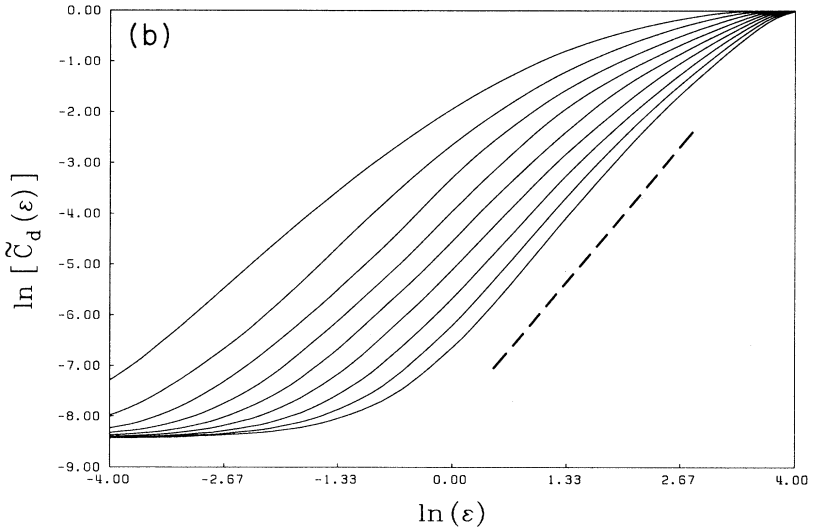

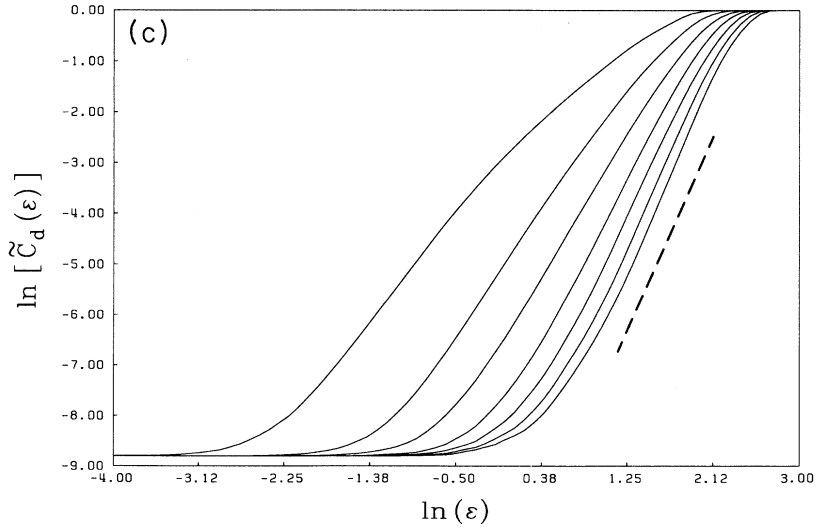

FIG. 8. Correlation functions in the (a) periodic ($p=0.7$), (b) quasiperiodic ($p=1.2$), and (c) chaotic ($p=1.248$) regimes. The convergence of the correlation function for different embedding dimensions is depicted. The slope of the straight dashed lines correspond to the correlation dimension D_c and leads to the following values: (a) $D_c=1$; (b) $D_c=2$; (c) $D_c=4.38$.

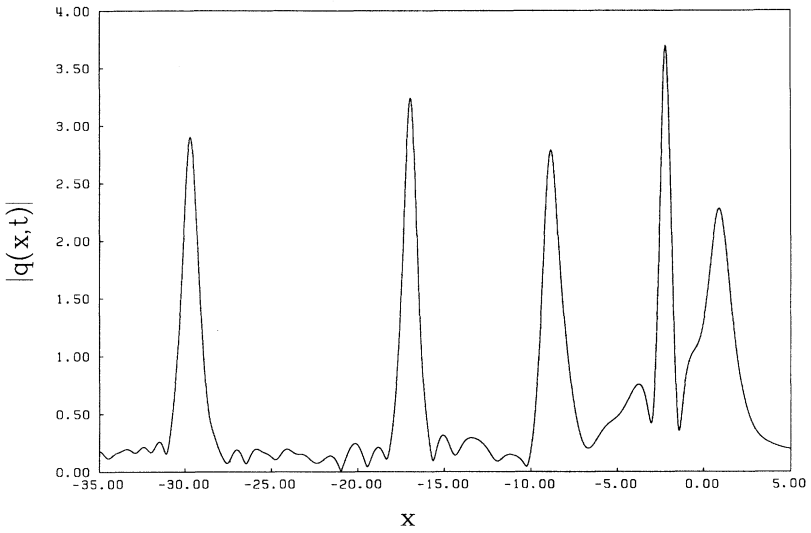

FIG. 9. Numerical solution $|q|$ at a fixed time t and $p=1.225$.

ation measured in the L_2 norm of the difference of the functions is less than 5%. Therefore the solution of the DNLIS equation in the convective region is the N-soliton solution of the corresponding integrable NLIS equation.

In the creation region near the critical density, the identification of solitons and the calculation of the soliton parameter is not so easy as in the convective region. To expand the solution of the DNLIS equation in terms of N-soliton solutions, we perform a nonlinear diagnostic by an algorithm based on the inverse scattering transform and a Downhill-Simplex algorithm. The diagnostic with IST, for the first time presented in Ref. [24], to our knowledge, was previously used successfully [25] for other types of disturbed NLS equations. Let us briefly review the IST for the integrable case of the NLS equation

$$i\partial_t q+\partial_x^2 q+2|q|^2 q=0 \ . \tag{49}$$

The initial value problem of (49) has a unique global solution if the L_2 norm of q and $\partial_x q$ is finite [26,27]. The solution of (49) is interpreted as a potential in the Zakharov-Shabat scattering problem [28]

$$\partial_x \mathbf{v}(x,t)=\begin{bmatrix} -i\zeta & q(x,t) \\ -q^*(x,t) & i\zeta \end{bmatrix}\mathbf{v}(x,t) \ . \tag{50}$$

The time evolution of the scattering data (e.g., ζ) is described by ordinary differential equations, for which the initial values at $t=0$ are calculated from (50). Solving these ordinary differential equations for $t>0$ one can construct the solution of (49) from the scattering data at $t=0$ [29].

For the diagnostic with the IST we only need the scattering data. Therefore, we define two pairs of linear independent solutions ϕ, $\bar{\phi}$ and ψ, $\bar{\psi}$ of the scattering problem (50) by their asymptotic behavior

$$\phi\sim\begin{bmatrix}+1\\0\end{bmatrix}e^{-i\zeta x} \ , \quad \bar{\phi}\sim\begin{bmatrix}0\\-1\end{bmatrix}e^{+i\zeta x} \ \text{ for } x\to-\infty \tag{51}$$

and

$$\psi\sim\begin{bmatrix}0\\+1\end{bmatrix}e^{i\zeta x} \ , \quad \bar{\psi}\sim\begin{bmatrix}+1\\0\end{bmatrix}e^{-i\zeta x} \ \text{ for } x\to+\infty \ . \tag{52}$$

The transformation matrix (or scattering matrix)

$$\begin{bmatrix}\phi\\ \bar{\phi}\end{bmatrix}=\begin{bmatrix}a(\zeta) & b(\zeta)\\ \bar{b}(\zeta) & -\bar{a}(\zeta)\end{bmatrix}\begin{bmatrix}\bar{\psi}\\ \psi\end{bmatrix} \tag{53}$$

between $\phi,\bar{\phi}$ and $\psi,\bar{\psi}$ defines the scattering data $a,\bar{a},b,\bar{b}$. In addition to the continuous spectrum (ζ real), there exist discrete eigenvalues $\zeta_k=\xi_k+i\eta_k$, $(k=1,\ldots,N)$ which are the complex zeros

$$a(\zeta_k,t)=0 \tag{54}$$

of the analytic continuation of the scattering coefficient a into the upper half plane. The set of scattering data

$$\{S(t)\}\equiv\{[\beta,\zeta \text{ real}];[\zeta_k,b_k]_{k=1}^N\} \ , \tag{55}$$

with $\beta=b(\zeta)/a(\zeta)$ for ζ real and

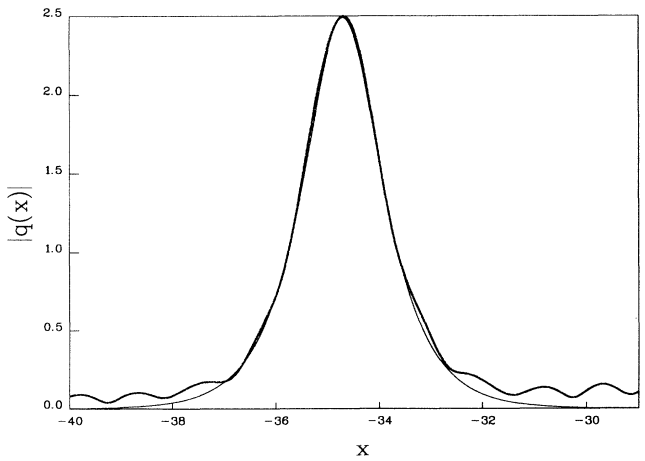

FIG. 10. Numerical solution (bold line) and the one-soliton solution (thin line) as followed from diagnostic with IST.

$b_k=\phi(\zeta_k,x,t)\psi^{-1}(\zeta_k,x,t)$, contains all necessary information to reconstruct the potential $q(x,t)$ for all times $t>0$ [28].

If we use the IST as a diagnostic tool for nonintegrable systems, it is sufficient to know the discrete eigenvalues ζ_k and the scattering coefficients b_k and $a(\zeta,t)$, from which one can calculate in principle the amplitudes, widths, positions, and phases of the solitons. If, for example, the spectrum contains one and only one discrete eigenvalue $\zeta_1=\xi_1+i\eta_1$, the potential $q(x,t)$ is a soliton of type

$$q_s=2\eta_1\mathrm{sech}[2\eta_1(x+2\xi_1 t-x_0)] \times\exp\{i[-2\xi_1 x+4(\eta_1^2-\xi_1^2)t+\varphi_0]\} . \quad (56)$$

The position x_0 and the phase φ_0 are given by

$$x_0=\ln\left[\frac{|C_0|}{2\eta_1}\right] \quad (57)$$

and

$$\varphi_0=\arg(C_0) , \quad (58)$$

respectively, with

$$C_0=\frac{b_1(\zeta_1)}{\partial_\zeta a|_{\zeta=\zeta_1}}e^{-2i\zeta_1 t} . \quad (59)$$

The explicit form of the N-soliton solution of (49) is more complicated and was for the first time given by Hirota [23], to our knowledge.

To analyze the dynamics of the DNLIS equation in the creation region we insert the solution $q(x,t)$ into the scattering problem (50). Solving (50) numerically we obtain $a(\zeta,t)$ and $b_k(\zeta,t)$ and from the solution of (54) we get ζ_k. Due to the reasons that the NLIS equation is invariant under translations in time and that the transformation from the NLIS equation to the NLS equation (49) for $t=0$ is

$$q_{\mathrm{NLS}}(x,0)=\left[\frac{p}{2}\right]^{1/2} q_{\mathrm{NLIS}}(x,0) , \quad (60)$$

it is sufficient to solve the scattering problem (50) for the NLS equation [instead of the scattering problem for the NLIS equation].

A good measure of the quality of the procedure described above is the L_2 norm of the deviation of the numerical solution q_{DNLIS} from the analytic N-soliton solution $q_{N\mathrm{sol}}$,

$$F(t)=\frac{\int_{X_R}^{X_L} dx\,|q_{\mathrm{DNLIS}}(x,t)-q_{N_{\mathrm{sol}}}|^2}{\int_{X_R}^{X_L} dx\,|q_{\mathrm{DNLIS}}(x,t)|^2} . \quad (61)$$

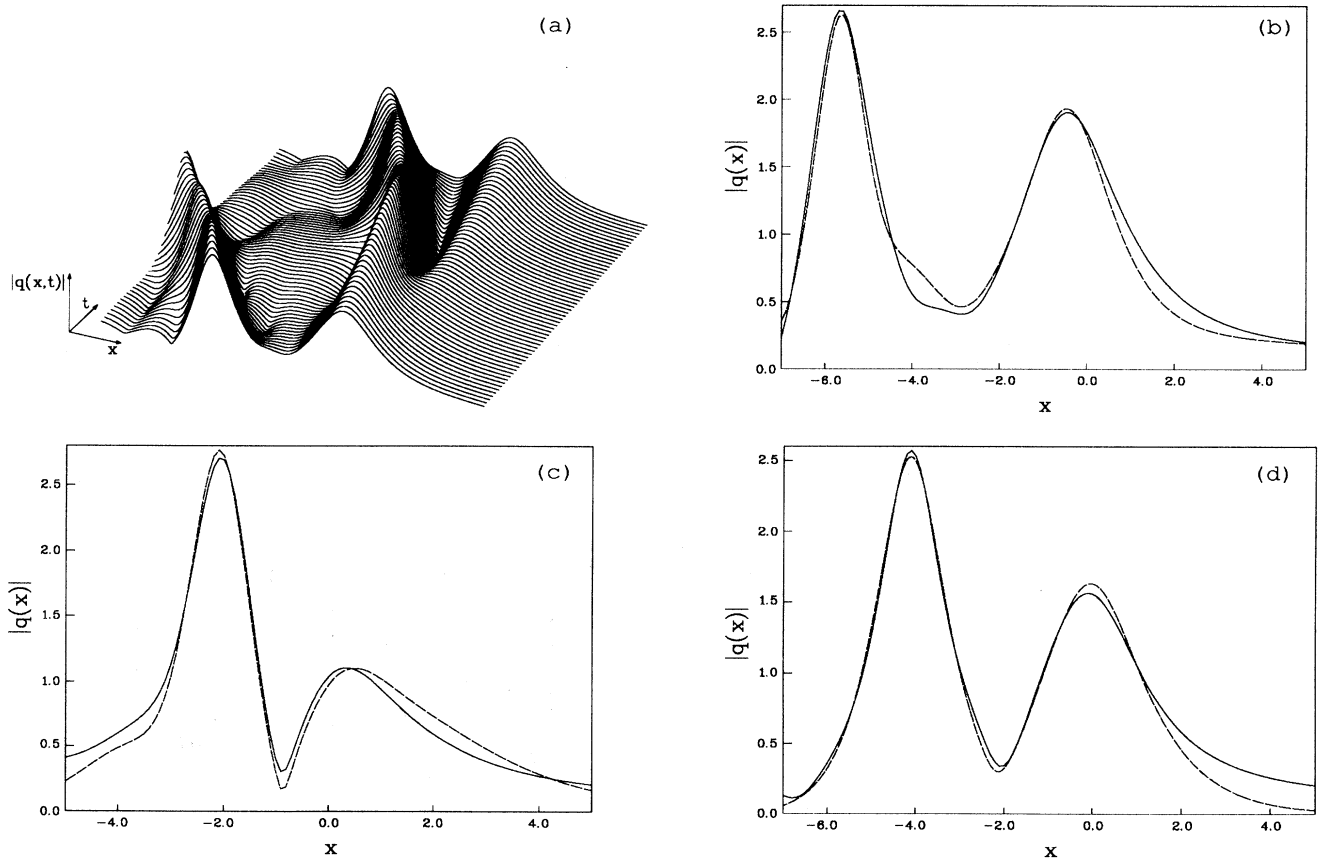

FIG. 11. (a) Space-time-plot of a numerical solution (absolute value of q) for one period at $p=0.7$. (b)–(d) Absolute value of q for numerical solution (solid line) and N-soliton solution (dashed line) for (a) $t=0.03$; (b) $t=1.01$; (c) $t=1.5$.

From the IST we get a rough estimate of the eigenvalues $\zeta_k(t_i)$, the positions $x_{0k}(t_i)$, and the phases $\varphi_{0k}(t_i)$ for the soliton k at time t_i. With these values we enter a Downhill-Simplex algorithm [12] to minimize the error (61). In addition we check the deviation in energy, which is given by

$$F_E = \frac{\int_{X_L}^{X_R} dx\,(|q_{\mathrm{DNLIS}}|^2 - |q_{N_{\mathrm{sol}}}|^2)}{\int_{X_L}^{X_R} dx\,|q_{\mathrm{DNLIS}}|^2} . \tag{62}$$

The minimization leads to an error $F<8\%$ in the L_2 norm and $F_E<8\%$ in energy. Thus we have found a qualitatively good method to expand the numerical solution of the DNLIS equation in terms of solitons of the corresponding integrable equation.

Now we present some results of the diagnostic for the periodic case at $p=0.7$. The single solitons of the N-soliton solution are labeled by S_k and the corresponding soliton parameter by $\zeta_k=\xi_k+i\eta_k$, x_{0k} and $\varphi_{0k}(k=1,2,3,\ldots)$ The space-time plot of the numerically obtained solution is depicted in Fig. 11 for one period $T=1.75$. Figures 11(b)–11(d) show the solutions $|q(x,t)|$ at $t=0.03$, 1.01, and 1.5.

From the diagnostic we obtain the dynamic of the soliton parameter as plotted in Fig. 12. For $t=0$ there are two well-separated solitons in the interval $[-10,5]$. The behavior of the eigenvalue of soliton S_1 (at $x_{01}\approx -5$) shows the characteristic dynamic of a soliton in the convective region, namely, weak oscillation of amplitude η_1 and a linear increasing of ξ_1 with time t [see Figs. 12(a) and 12(b)].

At time $t\approx 0.03$ a new soliton (S_3) is created at the position $x_{02}\approx -0.6$ of the old soliton S_2. The real part of the new soliton $\xi_3=0.14$ is finite and the phase φ_{03} is between π and 2π. [see Figs. 12(b) and 12(d)]. During the growth of the soliton S_2 near the critical density at $x\approx 0$, the newly created soliton S_3 moves in the overdense region up to $x_{03}\approx 2.5$ [see Fig. 12(c)] with nearly constant phase φ_{03} [see Fig. 12(d)]. Now the phase φ_{03} decouples from the driver, the soliton S_3 starts its journey down the density gradient into the convective region [see Fig. 12(c)], and the amplitude η_{03} increases rapidly to its asymptotic value [see Fig. 12(a)]. In the distribution function $|q(x,t\approx 1.01)|$ the solitons S_2 and S_3 are separated and the soliton S_1 leaves the interval $[-10,5]$ [see Fig. 11(c)]. At $t\approx 1.4$ the soliton S_2 leaves the creation region and at $t\approx 1.76$ one period is finished.

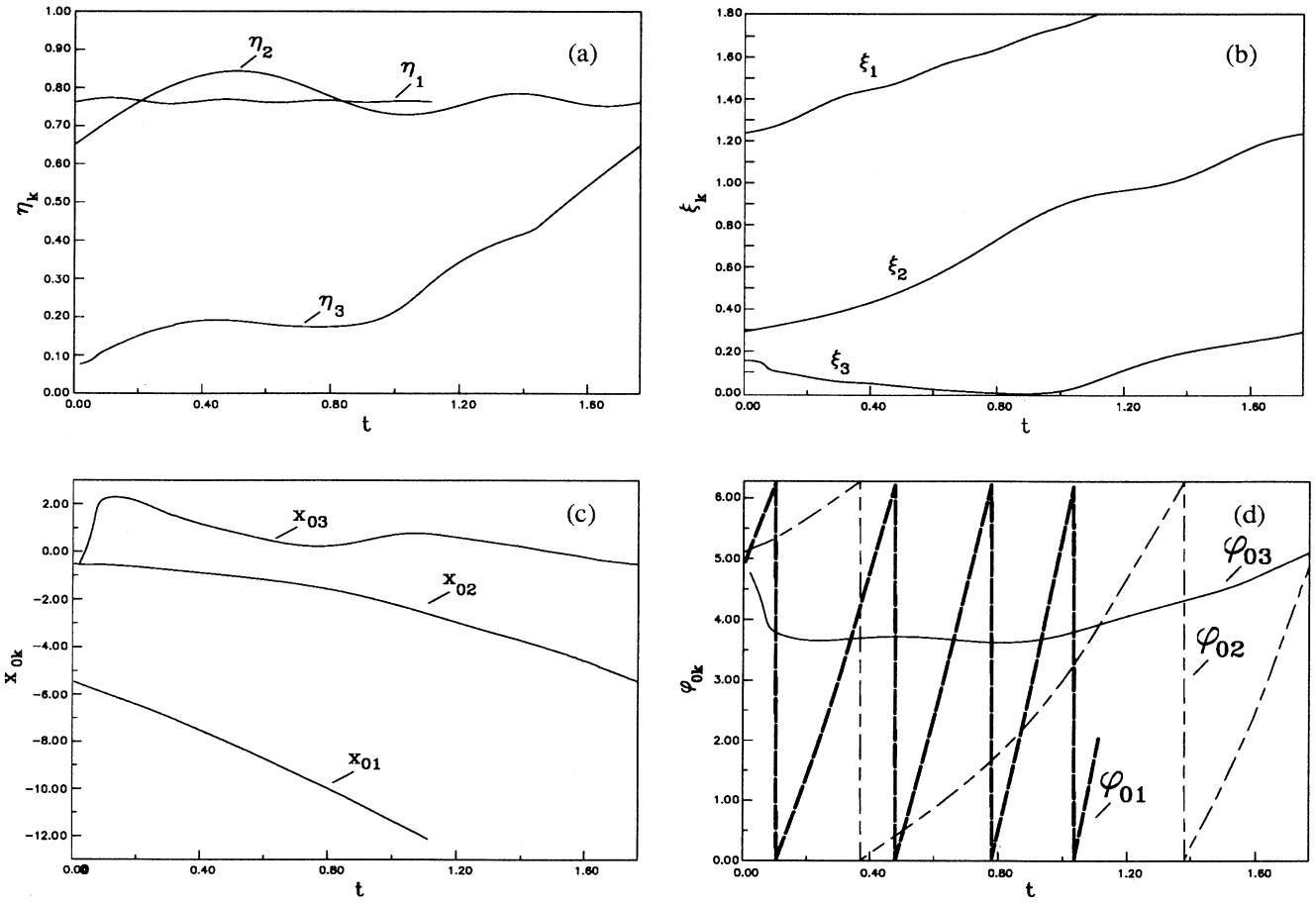

FIG. 12. Dynamic of soliton parameters for $p=0.7$. (a) Imaginary parts of the eigenvalues, (b) real parts of the eigenvalues, (c) positions, and (d) phases of the solitons.

This diagnostic was done for various values of the parameter p. The characteristic behavior described above holds for all parameters, except in the two-periodic regime where, instead of the two-soliton solution, a three-soliton solution in the creation region was observed.

Thus we have shown that the observed pulses in the DNLIS equation are the solitons of the corresponding integrable NLIS equation. In the convective region these solitons are well separated, whereas in the creation region near the critical density an interaction of several solitons takes place. New solitons are generated at the position of the rightmost soliton with finite real parts of ζ.

V. A LOW-DIMENSIONAL MODEL FOR CHAOTIC SOLITON GENERATION

The numerical solutions of the DNLIS Eq. (42) suggest to describe the transition from periodic soliton generation to chaotic behavior in time by a finite-dimensional model. In this section we construct in two steps a low-dimensional model, which is based on the soliton solutions of the integrable NLIS Eq. (43). In the first step, we derive in the creation region a system of coupled ordinary nonlinear differential equations for time-dependent parameters (the so-called "collective coordinates") of a solitary structure. In the second step a nonlinear map is formulated, which describes the generation of solitons at the critical density.

By the method of collective coordinates the dynamics of a partial differential equation is (approximately) reduced to a finite set of ordinary differential equations. The success of this method depends strictly on the chosen trial functions, which are solutions of the corresponding integrable equation.

For the generalized DNLIS equation

$$i\partial_t q+\partial_x^2 q+p|q|^2 q=\alpha x q+\beta \ , \tag{63}$$

we choose the trial function

$$q(x,t)=\left[\frac{2}{p}\right]^{1/2} A(t)f(x,t)e^{i\phi(x,t)} \tag{64}$$

with

$$f(x,t)=\mathrm{sech}\{B(t)[x-x_0(t)]\} \tag{65}$$

and

$$\phi(x,t)=k(t)[x-x_0(t)]+\varphi_0(t) \ . \tag{66}$$

The motivation for (63) is the following. First, (63) contains the exact solution of the integrable NLS equation ($\alpha=\beta=0$), if $A(t)=B(t)=2\eta$, $x_0(t)=4\xi t+x_0(0)$, $k(t)=-2\xi$, and $\varphi_0(t)=4(\eta^2-\xi^2)t+\varphi_0(0)$. In addition, we can model with $A(t)$ and $B(t)$ solutions whose energies are higher than those of a single soliton. Here the integral part of the ratio $N=A/B$ specifies the number of solitons of the NLS initial value problem [30].

There exist several methods to derive a closed set of ordinary differential equations for the set of parameters $\{A,B,k,x_0,\varphi_0\}$. Here, the "variation-of-action method" (VAM) [31] does not lead to satisfactory results, since one ends up with a relation between amplitude A and inverse width B, which forbids solutions which differ from the one soliton of the unforced equation. To bypass this problem, Larroche *et al.* [32] introduce a larger test function space by a so-called "chirp" in the phase $\phi(x,t)$ being proportional to $[x-x_0(t)]^2$. The results are effectively the same as in the paper of Bussac *et al.* [33]. The authors of the latter paper used a different method to derive a low-dimensional system, which is a mixture of the "momentum method" and a local approximation of the partial differential equation. Due to the fact that they did not average over the whole space their results describe only a small part of the whole dynamics, namely the periodic soliton emission.

To derive a more general map let us start from the momentum method. We use the first three conserved quantities of the integrable NLS equation ($\alpha=\beta=0$), i.e., the density

$$I_0\equiv\int_{-\infty}^{+\infty} dx\,|q(x,t)|^2=\text{const} \ , \tag{67}$$

the momentum

$$I_1\equiv i\int_{-\infty}^{+\infty} dx\,\{q\partial_x q^*-q^*\partial_x q\}=\text{const} \ , \tag{68}$$

and the energy

$$I_2\equiv\int_{-\infty}^{+\infty} dx\left\{\frac{p}{2}|q|^4-|\partial_x q|^2\right\}=\text{const} \ . \tag{69}$$

In addition, we incorporate the "center of mass"

$$M_s(t)=\int_{-\infty}^{+\infty} dx\,\{x|q|^2\} \tag{70}$$

and the "phase"

$$M_\phi(t)=\int_{-\infty}^{+\infty} dx\,\{|q|^2\partial_t\phi\} \ . \tag{71}$$

Clearly, in the case of the DNLIS equation ($\alpha\neq 0$ and $\beta\neq 0$), the quantities I_0, I_1, and I_2 are not constants of motion. Instead we obtain the following system of equations:

$$\frac{d}{dt}I_0=i\beta\int_{-\infty}^{+\infty} dx\,\{q^*-q\} \ , \tag{72}$$

$$\frac{d}{dt}I_1=-2\alpha I_0 \ , \tag{73}$$

$$\frac{d}{dt}I_2=\alpha I_1+i\beta\int_{-\infty}^{+\infty} dx\,\{p|q|^2(q-q^*)\} \ , \tag{74}$$

$$\frac{d}{dt}M_s=I_1+i\beta\int_{-\infty}^{+\infty} dx\,\{x(q-q^*)\} \ , \tag{75}$$

$$\frac{d}{dt}M_\phi=I_2-\alpha M_s+\tfrac{1}{2}\int_{-\infty}^{+\infty} dx\,\{p|q|^4-\beta(q+q^*)\} \ . \tag{76}$$

Inserting the trial function (64) in the system (72)–(76), we end up with equations of motion for the collective coordinates $\{A,B,k,x_0,\varphi_0\}$. For the later discussions it is very useful to introduce the new collective coordinates "soliton number" $N(t)$ and "energy" $M(t)$:

$$N(t)=\frac{A(t)}{B(t)} \ , \quad M(t)=\frac{4A^2(t)}{pB(t)} \ . \tag{77}$$

One gets the following system of coupled nonlinear equations of motion for the set $\{N,M,k,x_0,\varphi_0\}$:

$$\frac{d}{dt}N=-\beta\frac{3\pi}{\sqrt{2p}}\frac{N^2}{M}\left[1-\frac{16k^2N^4}{p^2M^2}\right]\sin(\varphi_0)\mathrm{sech}(I)\ , \tag{78}$$

$$\frac{d}{dt}M=-\beta\frac{4\pi}{\sqrt{2p}}\sin(\varphi_0)\mathrm{sech}(I)\ , \tag{79}$$

$$\frac{d}{dt}k=\beta\frac{4\pi}{\sqrt{2p}}\frac{kN}{M}\sin(\varphi_0)\mathrm{sech}(I)-\alpha\ , \tag{80}$$

$$\frac{d}{dt}x_0=2k-\beta\frac{16\pi^2}{(2p)^{3/2}}\frac{N^3}{M^2}\cos(\varphi_0)\mathrm{sech}(I)\tanh(I)\ , \tag{81}$$

$$\frac{d}{dt}\varphi_0=k^2-\alpha x_0-\frac{p^2}{48}\frac{M^2}{N^4}(1-4N^2) -\beta\frac{2\pi}{\sqrt{2p}}\frac{N}{M}\cos(\varphi_0) \times\mathrm{sech}(I)\left[1+\frac{4\pi kN^2}{pM}\tanh(I)\right]\ , \tag{82}$$

where we used the abbreviation $I\equiv 2\pi kN^2/pM$.

If we decouple the system from the driver by setting $\beta=0$, Eqs. (78)–(82) can be solved, and we obtain

$$A=B=\text{const}\ , \tag{83}$$

$$k(t)=-t+k(0)\ , \tag{84}$$

$$x_0(t)=-t^2+2k(0)t+x_0(0)\ , \tag{85}$$

$$\varphi_0(t)=\tfrac{2}{3}t^3-2k(0)t^2+[B^2(t)+k^2(0)]t -x_0(0)t+\varphi_0(0)\ . \tag{86}$$

With this time dependence of the collective coordinates, the test function (64) is exactly the one-soliton solution of the NLIS Eq. (43). From the numerics it is clear that the pulses converge in the convective region to that form.

In the case of the full DNLIS Eq. (63) we solve the complete system (78)–(82) with a Kutta-Merson algorithm [34]. The main difficulty is the choice of the initial values for the collective coordinates $\{N,M,k,x_0,\varphi_0\}$. With the results of the IST diagnostic, presented in the last section, we are able to fix the initial conditions, which are nearest to the numerical solution. Due to the invariance under time translations we choose $t=0$. As described before, a new soliton is generated at the position of the preceding soliton; so in general $x_0(0)\neq 0$. For the x-dependent part of phase ϕ we set, in agreement with the results of the simulation, $k(0)x_0(0)\approx 0.08$. The lowest detected value of the imaginary part η of the eigenvalue ζ supplies the initial value for the inverse width $B(0)\approx 2\eta(0)\approx 0.2$.

Together with the amplitude A the energy of the numerical solution increases after the generation of a soliton. In our low-dimensional model, the energy $M(t)$ follows from

$$\frac{d}{dt}M\approx-\sin(\varphi_0)\ , \tag{87}$$

which shows that initially the phase $\varphi_0(0)$ has to be in the range $\pi<\varphi_0<2\pi$.

A characteristic time evolution of the collective coordinates is shown in Fig. 13. The typical increase of both, the energy M and the inverse width B, is clearly seen. In agreement with the results of the numerical simulation, the position of the soliton x_0 first moves into the overdense region of the plasma ($x>0$), and the phase φ_0 is nearly constant. At later times $t>2$, the phase shows the expected asymptotic behavior in the convective region.

Although we started with $N(0)=1$ (one soliton), the soliton number is not conserved. It converges to an asymptotic value $N_\infty>1$. This reveals the fact that the test function (64) describes, at least very roughly, a multisoliton solution.

In the second step we derive, based on the results of the IST diagnostic of the numerical simulation, a nonlinear map, which describes the successive generation of solitons at the critical density near $x=0$. The main idea is to construct (at the end of the creation of one soliton at $t=t_e$) from the set of the collective coordinates $\{N(t_e),M(t_e),k(t_e),x_0(t_e),\varphi(t_e)\}$ a new set $\{N(t_0),\dots\}$ of initial conditions and solve again the system of equations of motion. If we call the solution of the system (78)–(82) $\{S^i(t)\}$ [for the initial conditions $\{S^i(t_0^i)\}$], the nonlinear map T can be formally written as

$$\{S^{i+1}(t_0^{i+1})\}=T(\{S^i(t_e^i)\})\ . \tag{88}$$

If, e.g., the map (88) converges to a fixed point, the low-dimensional model describes the periodic soliton generation and emission.

The procedure discussed above is similar to a method firstly presented by Shaw [35], to our knowledge, for the description of a dripping leaky faucet. There we also have a slow increase of the water drops and an abrupt breakoff. Similarly, here the emission phenomena of the solitons are so short in comparison with the time needed for their generation that an energy transfer between the driver and the solution plays a negligible role. Therefore the description of the instantaneous emission of solitons by a map, which implies a vanishing emission time, is in good agreement with the numerical simulation. Based on this procedure Bussac *et al.* [33] also constructed a map, which can only model periodic soliton generation for all values of $p>0.25$. Larroche and Pesme [36] examined the model of Larroche *et al.* [32] and found a periodic and a two-periodic regime, but there is no quantitative agreement of the bifurcation values with the numerics, and the model fails to describe chaotic soliton generation at the critical density. In our opinion, the main reasons for this failure are the pinning of the position of soliton generation to a value $\bar{x}=0$ (in their notation, where $\bar{x}$ is the position of the soliton in its rest frame), the setting of the linear x-dependent phase equal to zero in contradiction to the numerical results, and the adding of a chirp in the phase proportional to x^2. The latter is necessary for them because they use the variation-of-action method, for which the trial function without chirp leads to a strong coupling of amplitude and width.

To avoid these difficulties and to construct a consistent

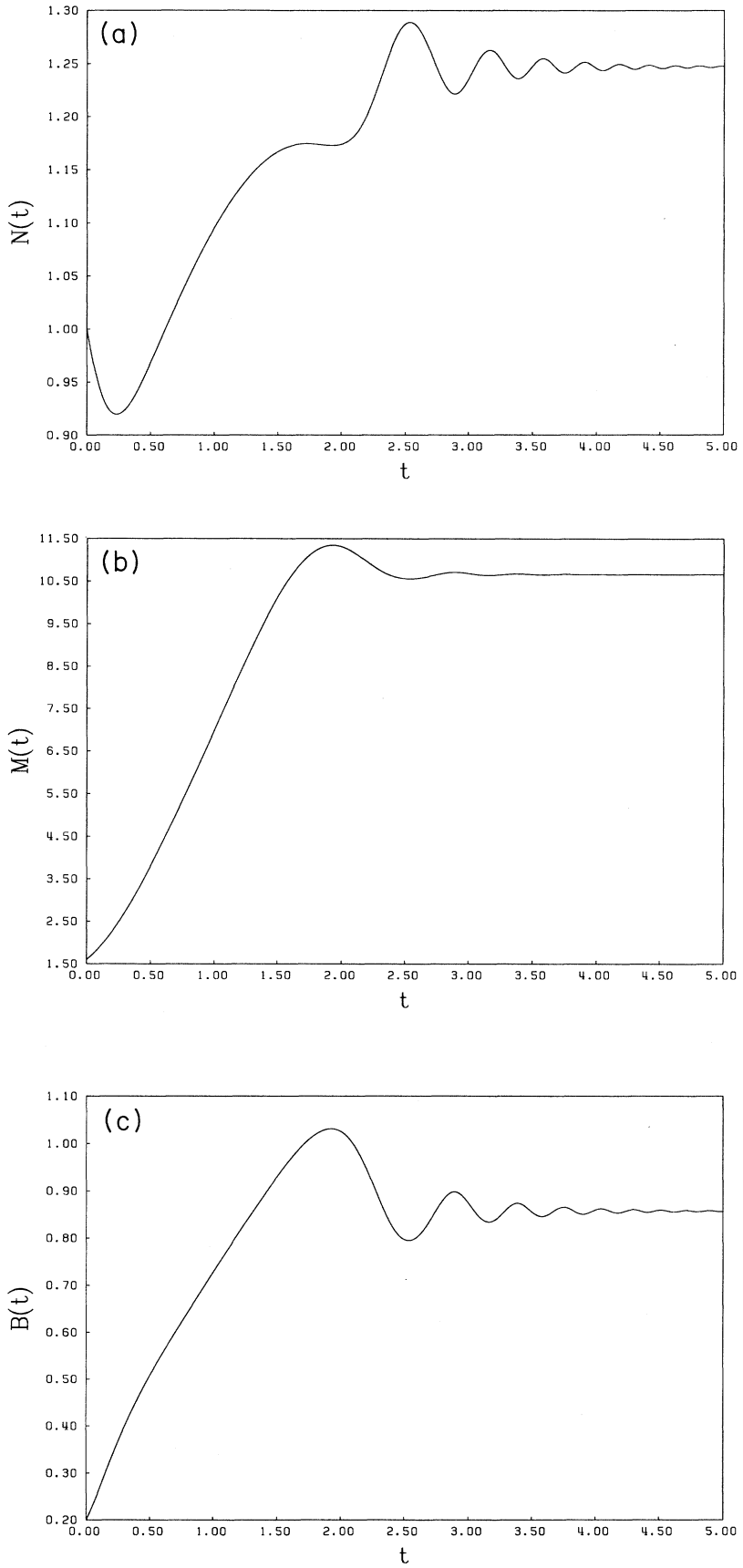

FIG. 13. Dynamic of the collective coordinates $N(t)$ soliton number, $M(t)$ soliton energy, $B(t)$ inverse soliton width, x_0 soliton position, and φ_0 space-independent soliton phase.

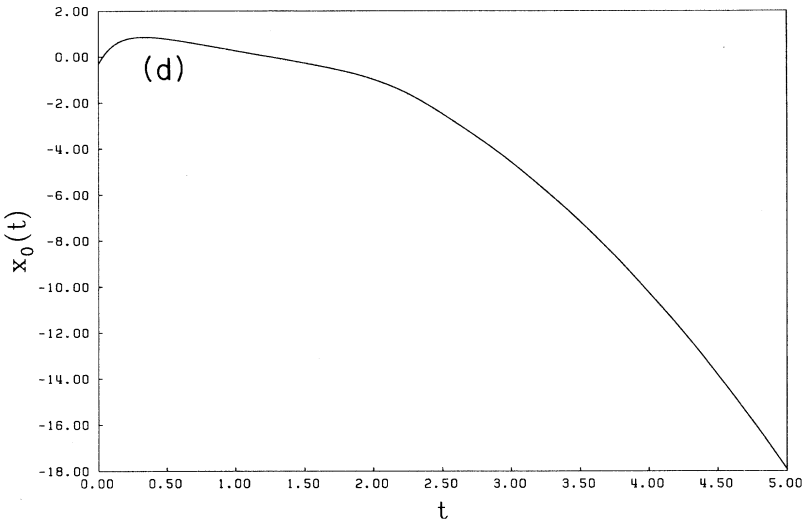

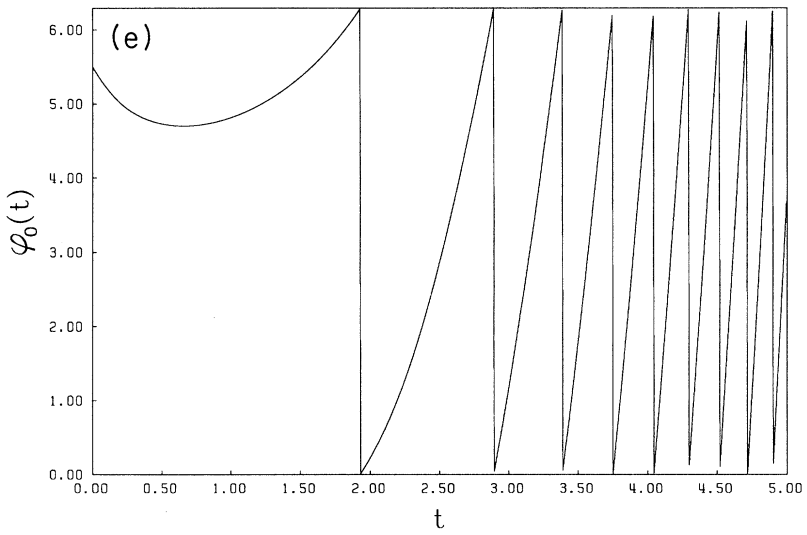

FIG. 13. (*Continued*).

model we refer to the results of the diagnostic with IST presented in Sec. IV. According to the invariance under time translations we set, without loss of generality, $t_0^i=0$ for all i. The definition of the emission time is in principle impossible from the numerical simulation. Due to this reason we identify the emission time t_e^i with the time t_c, i.e., the time of the maximum value of the energy for the generated solitons. Starting at $t=0$ with $B(0)=B_0\approx 2\eta(0)$ and $\varphi_0(0)=\varphi_{00}$, the energy $M(t)$ increases and reaches its maximum value at $t=t_c=t_e^i$, defined by

$$\left.\frac{d}{dt}M\right|_{t=t_e^i}=0\ ,\quad \left.\frac{d^2}{dt^2}M\right|_{t=t_e^i}<0\ . \tag{89}$$

From (89) and (79) one gets $\varphi_0(t_e^i)=2\pi$.

The emission of a soliton at $t=t_e^i$ is characterized by the reduction of the soliton number $N^{i+1}(t_0^{i+1})=N^i(t_0^i)-1$. This is equivalent to the reduction of the number of discrete eigenvalues ζ_k of the IST by one [30]. For the location of generation of a new soliton we use, in agreement with the numerical simulations, the position of the previous emitted soliton $x_0^{i+1}(t_0^{i+1})=x_0^i(t_e^i)$ and fix the product of the x-dependent phase with the position, i.e., $k^{i+1}(t_0^{i+1})x_0^{i+1}(t_0^{i+1})=C=\text{const}$. In summary we end up with the nonlinear map

$$\begin{pmatrix} N^{i+1}(t_0^{i+1}) \\ M^{i+1}(t_0^{i+1}) \\ k^{i+1}(t_0^{i+1}) \\ x_0^{i+1}(t_0^{i+1}) \\ \varphi_0^{i+1}(t_0^{i+1}) \end{pmatrix} = T \begin{pmatrix} N^i(t_e^i) \\ M^i(t_e^i) \\ k^i(t_e^i) \\ x_0^i(t_e^i) \\ \varphi_0^i(t_e^i) \end{pmatrix} = \begin{pmatrix} N^i(t_e^i)-1 \\ B_0[N^i(t_e^i)-1]^2 \\ C[x_0^i(t_e^i)]^{-1} \\ x_0^i(t_e^i) \\ \varphi_{00} \end{pmatrix} . \tag{90}$$

The phase space of the map (90) is of dimension three, namely $\{N,k,x_0\}$, and the parameter space is of dimension four $\{p,B_0,C,\varphi_{00}\}$. This is in contradiction to the DNLIS Eq. (42), which includes only one parameter p, and we therefore must fix a relation between B_0, C, φ_{00},

and p. Concerning this we choose the smallest detected value for the inverse width $B_0=0.2$. The constant $C=k^i(t_0^i)x_0^i(t_0^i)$ is set to the mean value observed in the IST diagnostic $C=0.13$. There is no strong qualitative dependence of the results on these values. In the ranges $0.05<B_0<0.4$ and $0.02<C<0.5$ we observe only a shift of the bifurcation points. (In contrast, the results are very sensitive to a change in the phase φ_{00}.) The nonlinear map converges only for values φ_{00} in the range $3\pi/2-0.8<\varphi_{00}<3\pi/2+0.8$. Due to the fact that there is no further indication from the numerical simulations we choose $\varphi_{00}=\text{const}=3\pi/2+C$. As initial conditions for the iteration we set always $N^0(t_0^0)=2$, $k^0(t_0^0)=0.16$, and $x_0^0(t_0^0)=0.5$.

With these settings we obtain the following behavior of the low-dimensional model. There exists a threshold $p_c=0.34$ for soliton generation. [Below this value, the soliton number $N^i(t_0^i)$ iterates to the unphysically value $\lim_{i\to+\infty}N^i(t_0^i)=-\infty$.] For small nonlinearities, there exist no solitons in agreement with the numerical simulation.

In the range $0.34<p<1.1$, the model converges within a few iterations to a fixed point (see Fig. 14), and describes the periodic soliton generation at the critical density near $x=0$. In Fig. 15 the period $T(p)$ is depicted for both the low-dimensional model and the DNLIS equation itself.

At $p\approx1.1$ the fixed point becomes unstable. The nonlinear map converges to two fixed points (Fig. 14) and we obtain, in agreement with the results of Sec. III, a subharmonic bifurcation. The new dynamical state of the system, being caused by a period doubling, is stable up to $p\approx1.18$.

Our low-dimensional model undergoes further subhar-

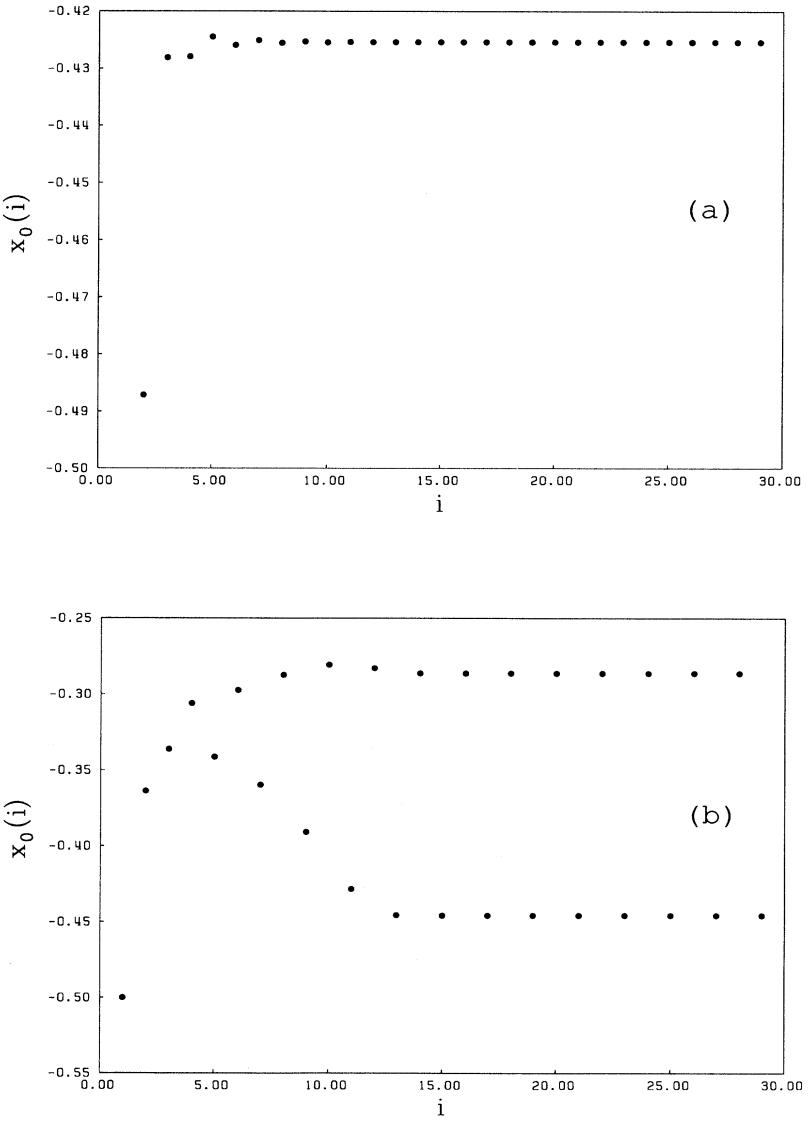

FIG. 14. Iteration of collective coordinate $x_0^i(0)$. (a) Periodic regime, (b) two-periodic regime.

monic bifurcations to periods 4, 8, and 16. This indicates the classical period-doubling route to chaos. The discrepancies between the model and the DNLIS Eq. (43) in the small-parameter range $1.18 < p < 1.23$ arises, in our opinion, from the fact that we choose a very special route through the four-dimensional parameter space $\{p, B_0, C, \varphi_{00}\}$. (This is similar to, e.g., fixing Ω and varying only K in the standard circle map [37]).

At $p \approx 1.23$ our low-dimensional model undergoes a bifurcation to a chaotic regime. Figure 16 shows exemplarily the results for the position $x_0^{i+1}(t_0^{i+1})$ versus $x_0^i(t_0^i)$ for $p = 1.24$. If we interpret the iteration results as values of a time series with time-step one, we obtain the Fourier spectrum depicted in Fig. 17.

The nonlinear map, presented in this section, is, to our knowledge, the first procedure that describes chaotic soliton generation within a low-dimensional model. This demonstrates first that the dynamics of the nonintegrable physical system is dominated by the solitons of the corresponding integrable equation, and second, that the whole dynamics can be described with a few degrees of freedom. The qualitative and quantitative good agreements between the numerical simulations and the low-dimensional model are shown in Fig. 18.

VI. SUMMARY

In this paper we have investigated the interaction of intense electromagnetic waves with inhomogeneous plasmas. Near the critical density, the resonant absorption of electromagnetic waves and the corresponding mode conversion to an electrostatic plasma wave can be described by the driven nonlinear inhomogeneous Schrödinger equation.

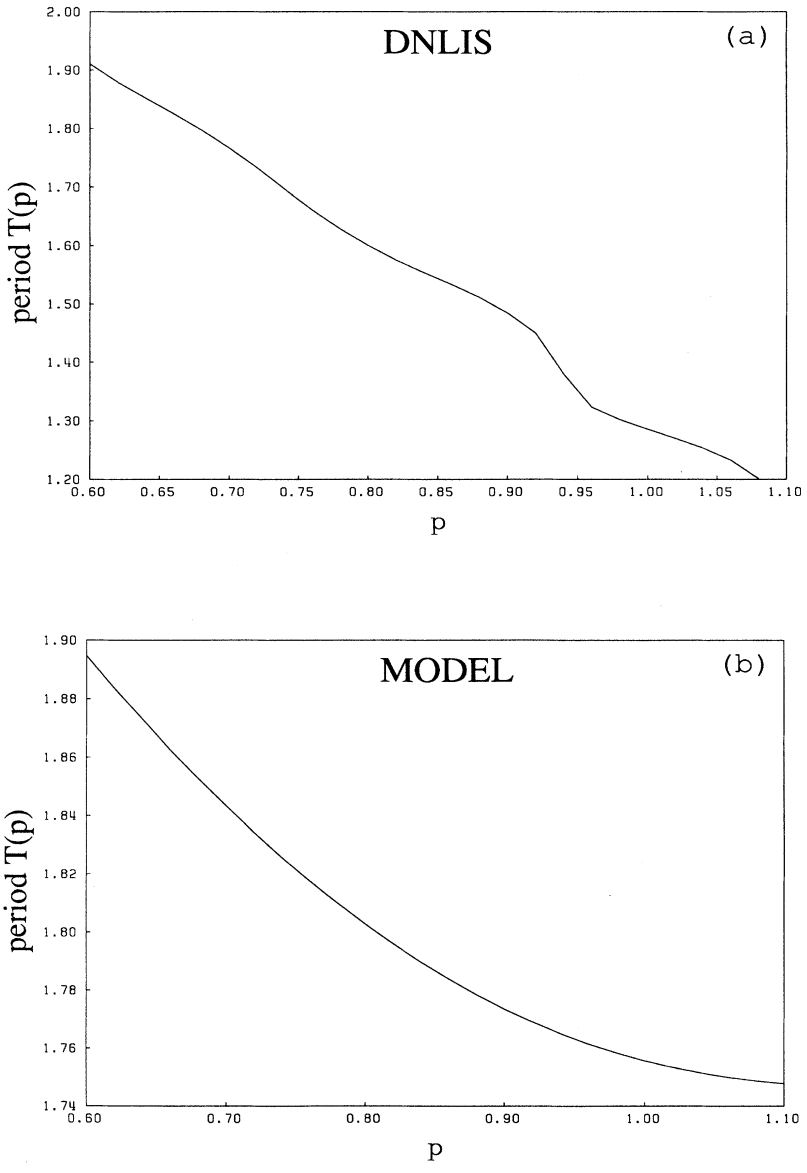

FIG. 15. Period time as function of bifurcation parameter p. (a) Numerical solution, (b) low-dimensional model.

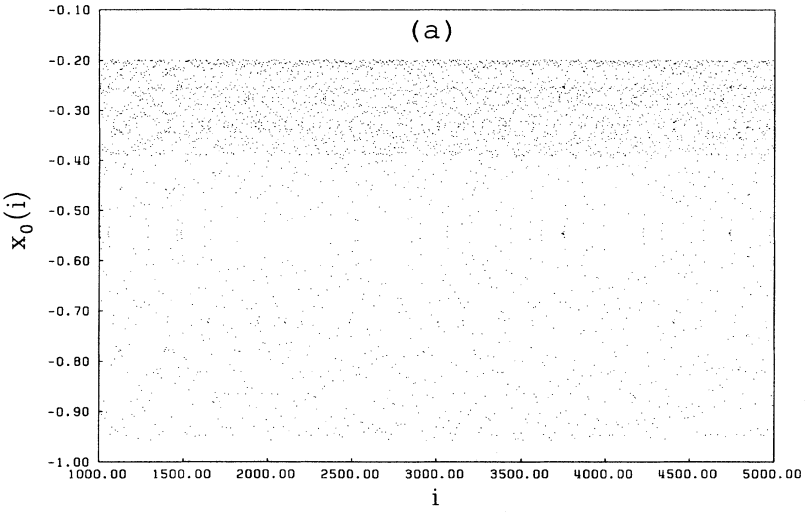

FIG. 16. Iteration of collective coordinate $x_0^i(0)$ in the chaotic regime. (a) Successive iterations, (b) chaotic attractor.

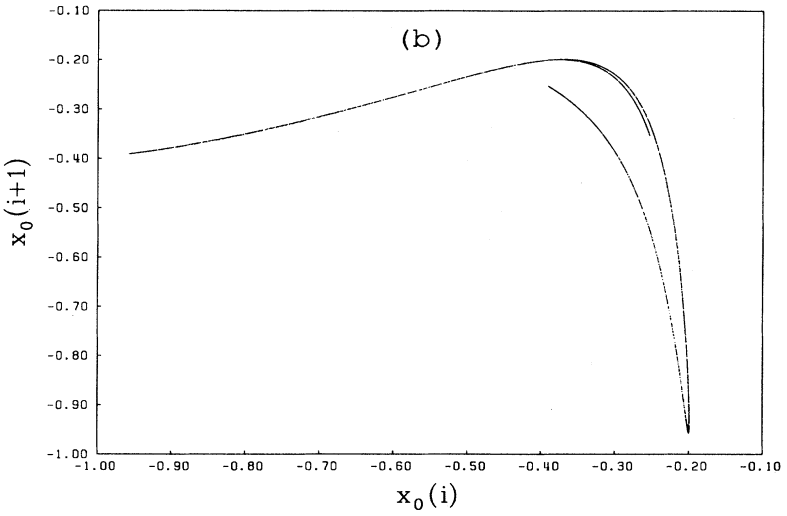

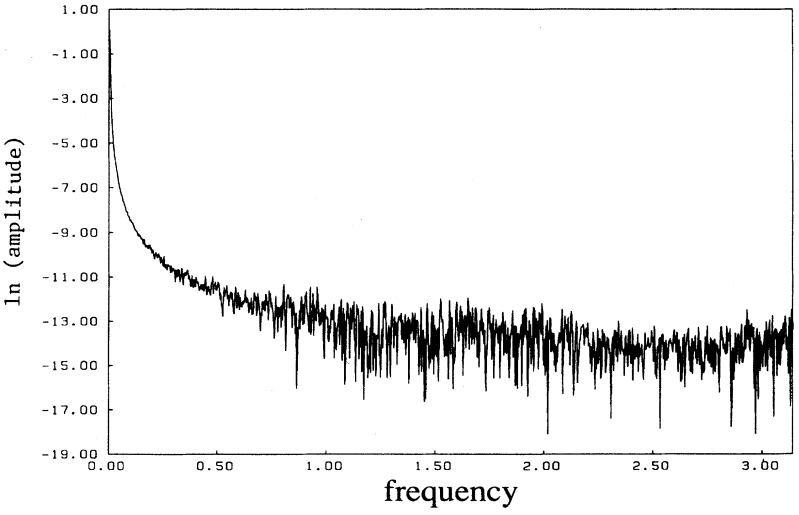

FIG. 17. Spectrum of the solution $x_0^{(i)}(0)$ depicted in Fig. 16.

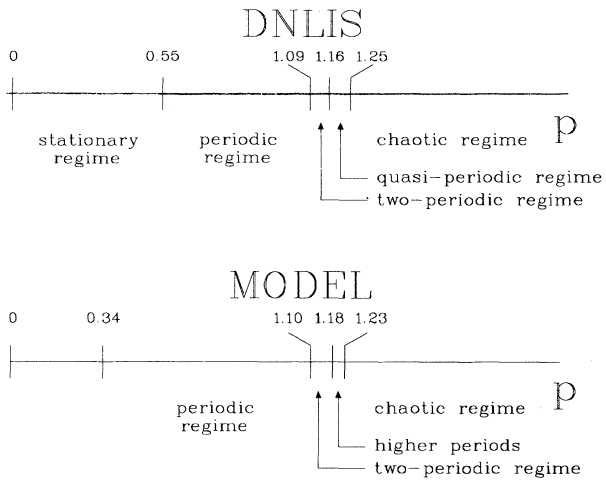

FIG. 18. Comparison between the numerical simulation of the DNLIS equation and the low-dimensional model.

By solving the DNLIS equation numerically, we studied the dynamics of the system in dependence on the control parameter p. The stationary Airy-type solution, for small values of p, in the near-linear case becomes unstable and bifurcates into a limit cycle. The spatial structure of the solution is dominated by separated pulses which are emitted periodically from the resonance point at the critical density. By further increasing p, one period doubling occurs. After that the Newhouse-Ruelle-Takens route to chaos via quasiperiodic pulse emission has been observed. We calculated the dimension of the chaotic attractor near the onset of chaos.

The spatial structure of the numerically observed solutions has been examined by a nonlinear diagnostic technique. For the latter we developed an algorithm, which is based on the inverse scattering transform for the NLIS equation, i.e., the corresponding integrable form of the DNLIS equation. We have shown that in the underdense plasma region the numerically observed pulses are the single-soliton solutions of the integrable NLIS equation. At the critical density, where the solitons are generated, the interaction of several solitons takes place. New solitons are generated at the position of the rightmost soliton with a nonvanishing x-dependent phase.

These results, together with the low attractor dimension in the vicinity of the transition to chaos, indicate the existence of a finite-dimensional model, which should describe the chaotic soliton generation. We derived a nonlinear map, which is based on the low-dimensional description of soliton dynamics by collective coordinates. Its qualitatively and quantitatively good agreement with the numerics demonstrates that the dynamics of the nonintegrable model is dominated by soliton solutions of the corresponding integrable equation. Moreover, these results show that the nonlinear mode conversion can be studied with the help of low-dimensional models. The method we presented here will be of use also for other soliton-generation problems.

[1] C. E. Max, *Laser Plasma Interaction,* edited by R. Balian and J. C. Adam (North-Holland, Amsterdam, 1982).
[2] R. L. Stenzel, A. Y. Wong, and H. C. Kim, Phys. Rev. Lett. **32**, 654 (1974).
[3] V. L. Ginzburg, *Propagaton of Electromagnetic Waves in Plasmas* (Pergamon, New York, 1970).
[4] N. G. Denisov, Zh. Eksp. Teor. Fiz. **31**, 609 (1957) [Sov. Phys. JETP **4**, 544 (1957)].
[5] Th. Speziale and P. J. Catto, Phys. Fluids **20**, 990 (1977).
[6] J. P. Freiberg, R. W. Mitchell, R. L. Morse, and L. I. Rudsinski, Phys. Rev. Lett. **28**, 795 (1972).
[7] J. C. Adam, A. Gourdin Serveniere, and G. Lavale, Phys. Fluids **25**, 376 (1982).
[8] B. Cros, J. Godiot, and G. Matthieussent, Phys. Fluids B **2**, 907 (1990).
[9] D. W. Forslund, J. M. Kindel, N. Lee, E. L. Lindmann, and R. L. Morse, Phys. Rev. A **11**, 679 (1975).
[10] V. E. Zakharov in *Basic Plasma Physics,* edited by A. A. Galeev and R. N. Sudan (Elsevier, New York, 1985), Vol. 2, p. 81.
[11] H. H. Chen and C. S. Liu, Phys. Rev. Lett. **37**, 693 (1976).
[12] W. H. Press, B. P. Flaunery, S. A. Teukolsky, and W. I. Vetterling, *Numerical Recipes* (Cambridge University Press, Cambridge, England, 1987).
[13] S. Newhouse, D. Ruelle, and F. Takens, Commun. Math. Phys. **64**, 35 (1978).
[14] H. G. Schuster, *Deterministic Chaos* (VCH, Weinheim, 1988).
[15] P. Grassberger and I. Procaccia, Phys. Rev. Lett. **50**, 346 (1983).
[16] P. Grassberger and I. Procaccia, Phys. Rev. A **28**, 2591 (1983).
[17] P. Grassberger, in *Chaos,* edited by A. V. Holden (Manchester University Press, Manchester, 1987).
[18] K. H. Spatschek, H. Pietsch, E. W. Laedke, and Th. Eickermann (unpublished).
[19] K. H. Spatschek, H. Pietsch, and E. W. Laedke, Europhys. Lett. **11**, 625 (1990).
[20] O. Larroche and D. Pesme (unpublished).
[21] W. Shyu, P. N. Guzdar, H. H. Chen, Y. C. Lee, and C. S. Liu, Phys. Lett. A **147**, 49 (1990).
[22] K. H. Spatschek, P. Heiermann, E. W. Laedke, V. Naulin, and H. Pietsch, in *Nonlinear Coherent Structures in Physics and Biology,* edited by M. Peyrard and M. Remoissenet, Lecture Notes in Physics Vol. 393 (Springer, Heidelberg, 1990), p. 219.
[23] R. Hirota, J. Math. Phys. **14**, 805 (1973).
[24] M. G. Forest and D. W. McLaughlin, J. Math. Phys. **23**, 1248 (1982)
[25] K. H. Sptschek, H. Pietsch, E. W. Laedke, and Th. Eickermann in *Singular Behavior and Nonlinear Dynamics,* edited by St. Pnevmatikos, T. Bountis, and S. Pnevmatikos (World Scientific, London, 1988), p. 555.
[26] J. Ginibre and G. Velo, J. Funct. Anal. **32**, 1 (1979).
[27] M. I. Weinstein, Commun. Math. Phys. **87**, 567 (1983).
[28] V. E. Zakharov and A. B. Shabat, Zh. Eksp. Teor. Fiz. **61**, 118 (1971) [Sov. Phys. JETP **34**, 62 (1972)].
[29] M. J. Ablowitz, D. J. Kaup, A. C. Newell, and H. Segur,

Stud. Appl. Math. **53**, 249 (1974).
[30] J. Satsuma and N. Yajima, Suppl. Prog. Theor. Phys. **55**, 284 (1974).
[31] Y. V. Katyshev and V. G. Makhankov, Phys. Lett. **57A**, 10 (1976).
[32] O. Larroche, M. Casanova, D. Pesme, and M. N. Bussac, *Laser Particle Beams,* **4**, *545 (1986).*
[33] M. N. Bussac, P. Lochak, C. Meunier, and A. Heron-Gourdin, Physica **17D**, 313 (1985).
[34] L. Fox and D. F. Mayers, *Computing Methods for Scientists and Engineers* (Clarendon, Oxford, 1968).
[35] R. Shaw, *The Dripping Faucet as a Model Chaotic System* (Aerial, Santa Cruz, 1984).
[36] O. Larroche and D. Pesme, in *Nonlinear and Chaotic Phenomena in Plasmas, Solids and Fluids,* edited by W. Rozmus and J. A. Tushyski (World Scientific, Singapore, 1991).
[37] P. Bak, T. Bohr, T. Jensen, and M. H. Christiansen, Solid State Commun. **51**, 231 (1984).